NASA Technical Memorandum 100177

Flaw Imaging and Ultrasonic Techniques for Characterizing Sintered Silicon Carbide

George Y. Baaklini
Cleveland State University
Cleveland, Ohio

and

Phillip B. Abel
Lewis Research Center
Cleveland, Ohio

Prepared for the
Conference on Nondestructive Testing of High-Performance Ceramics
cosponsored by the American Ceramic Society and
the American Society for Nondestructive Testing
Boston, Massachusetts, August 25–27, 1987

NASA

FLAW IMAGING AND ULTRASONIC TECHNIQUES FOR CHARACTERIZING SINTERED SILICON CARBIDE

George Y. Baaklini
Cleveland State University
Cleveland, Ohio 44115

and

Phillip B. Abel
National Aeronautics and Space Administration
Lewis Research Center 44135

ABSTRACT

This investigation assessed the capabilities of projection microfocus x-radiography, ultrasonic velocity and attenuation, and reflection scanning acoustic microscopy for characterizing silicon carbide specimens. Silicon carbide batches covered a range of densities and different microstructural characteristics. Room-temperature, four-point flexural strength tests were conducted. Fractography was used to identify types, sizes, and locations of fracture origins. Fracture toughness values were calculated from fracture strength and flaw characterization data. Detection capabilities of radiography and acoustic microscopy for fracture-causing flaws were evaluated. Applicability of ultrasonics for verifying material strength and toughness was examined.

E-3753

INTRODUCTION

Fracture mechanics plays an important role in the development of and the failure prediction for ceramic materials, but its application to structural reliability is limited in general by cost-prohibitive proof testing and by related shortcomings in duplicating a complex state of stresses (ref. 1). Hence, there exists the need for nondestructive testing which ensures that materials are free of detrimental defects, and which helps in ranking materials according to their predicted strength and toughness. It is therefore of prime interest to critically examine available nondestructive techniques for the evaluation of ceramic materials.

Substantial advances in nondestructive characterization and defect detection have been made through numerous flaw imaging techniques, including nuclear magnetic resonance (ref. 2), microfocus radiography (refs. 3 and 4), scanning laser acoustic microscopy (ref. 5), scanning acoustic

microscopy (ref. 6), and scanning photoacoustic microscopy (refs. 7 and 8). Most of these techniques were applied to materials with artificially seeded defects that simulate naturally occurring, fracture-causing flaws, either to assess flaw detectability or to establish the reliability of detection. This paper will examine the application of scanning acoustic microscopy and microfocus radiography to detection of naturally occurring, fracture-causing flaws in silicon carbide (SiC) ceramics. This will entail establishing or verifying the resolution of these systems needed for ceramic materials, and assessing whether further investigation of these techniques is merited.

Flexural strength and fracture toughness dependency on ceramic microstructure is well developed and documented in the literature (refs. 9 to 11). Recent studies (refs. 12 to 14) have shown that attenuation depends on the microstructure of SiC. Experimental correlations between ultrasonic attenuation and fracture toughness were established in metallic materials (ref. 15). A survey of the literature does not reveal any attempt to relate ultrasonic attenuation with fracture mechanics parameters in SiC ceramic systems. This paper will use destructive testing to determine four-point flexural strength and will use corresponding fractography analysis to calculate fracture toughness from the applied stress and from the size, shape, and location of fracture-causing flaws. This paper will assess, for the carbide systems under consideration, the influence of microstructure on attenuation, flexural strength, and fracture toughness, and will investigate the attenuation toughness/strength relationship.

EXPERIMENTAL PROCEDURE

Specimen Preparation

Twenty-five modulus of rupture (MOR) bars were prepared from -100-mesh α-SiC powder containing boron and carbonaceous resin binders. Compaction of the green specimen included dry pressing the powder by using a double-action, tungsten-lined die, vacuum sealing the green bars in thin-wall latex tubing, and cold isopressing the bars at 420 MPa. These bars represent five different batches (table I) which were sintered or sintered and hot isostatically pressed in order to tailor their density and microstructure. All bars were machined, the four long edges beveled, and further polished to a 0.07-μm rms surface finish. Nominal test bar dimensions were 2.72 by 5.58 by 31.71 mm.

TABLE I. - SINTERING AND HOT ISOSTATIC PRESSING CONDITIONS

Batch number	Sintering			Hot isostatic pressing			Density,[a] g/cm^3
	Temperature, °C	Time, hr	Argon pressure, MPa	Temperature, °C	Time, hr	Argon pressure, MPa	
1	2200	0.5	0.1	----	---	---	3.12
2HP	2200	1.5	↓	2100	0.5	138	3.14
4	2300	1.0		----	---	---	3.05
4HP	2300	1.0		2150	1.0	138	3.10
5HP	2100	.75		2100	1.0	138	2.92

[a] ± 0.01 g/cm^3.

Microstructural Characterization

Mean pore size, shape, and orientation were determined from photomicrographs of polished representative samples from each batch by applying two-dimensional Fourier transform theory (ref. 16). Mean grain size was determined from photomicrographs of polished and etched representative samples of each batch by using an interactive image analysis system, where grain boundaries could be traced at a digitizer tablet. Table II lists mean pore sizes, mean grain sizes, and their corresponding shapes for all five batches (ref. 13).

TABLE II. - CHARACTERIZATION OF MICROSTRUCTURE

Batch number	Density, g/cm^3	Mean grain size,[a] μm			Mean pore size,[a,b] μm			Grain shape
		Circle[c]	Ellipse[d]		Circle[e]	Ellipse[a,f]		
		Diameter	Major	Minor	Diameter	Major	Minor	
1	3.12	5.76	7.94	4.56	1.60	1.61	1.59	Equiaxed and elongated
2HP	3.14	6.75	9.61	5.15	1.63	1.75	1.50	Equiaxed and elongated
4	3.05	11.56	19.39	7.73	3.82	4.00	3.64	Elongated
4HP	3.10	11.18	18.08	7.82	3.44	3.60	3.27	Elongated
5HP	2.92	3.36	4.40	2.78	2.29	2.38	2.19	Equiaxed

[a]±0.2 μm.
[b]No preferred orientation.
[c]Assuming all grains are equiaxed.
[d]Assuming all grains are elongated.
[e]Calculated average from f.
[f]Real measurements off the mean shape.

Radiographic Evaluation

All specimens were film radiographed in order to detect potential fracture-causing flaws. The microfocus system used was operated in the projection mode (5X magnification) and in the 30 to 60 kV range with a beam current range of 0.25 to 0.32 mA. The system had a molybdenum anode and a 10-μm focal spot. All radiographs were manually developed, and were examined with the aid of a 7X optical measuring magnifier under variable-intensity backlighting (1000 to 9000 lm/m^2) in subdued room lighting. Test bars were radiographed in two modes, the (W,L) mode, where x-rays were transmitted through the thickness, and the (T,L), mode where x-rays were transmitted through the width, which when combined form a three-dimensional radiographic location of flaws.

Scanning Acoustic Microscopy Evaluation

The scanning acoustic microscope used was of the pulse-reflection type, operating with a reduced-aperture lens at a nominal 50-MHz center frequency. An acoustic lens positioned above the sample in a fluid coupling bath both generated and detected ultrasonic pulses. Stepper motors drove the sample in a raster pattern as the reflected signal amplitude was digitally stored as a function of position. An adjustable delay time between pulse generation and signal digitization allowed imaging of either surface or subsurface flaws which could cause fracture. A schematic diagram of the lens-specimen configuration is shown in figure 1.

Ultrasonic Evaluation

Velocity and attenuation measurements were determined for all samples through the thickness at three different locations in the highest stressed area of the test specimen, as indicated in figure 2. The pulse-echo technique, with a 100-MHz broadband longitudinal-wave transducer, was used to measure the cross correlation velocity (ref. 17) and the attenuation coefficient (ref. 18) from the first and second back surface reflections. The front surface reflections obtained with and without the bar in place were used to calculate the reflection coefficient of the buffer rod-couplant-sample interface. This frequency-dependent reflection coefficient was incorporated for precision attenuation measurements (refs. 13 and 18).

Testing and Fractography

Four-point flexural strength tests were conducted at a crosshead speed of 0.51 mm/min, with inner and outer spans of 9.53 and 19.05 mm, respectively. Tests were conducted in air at room temperature. Fracture surfaces were examined in a scanning electron microscope (SEM) to determine the location, size, and type of failure-initiating flaws. Fracture strengths at the tensile surface (σ_t) were calculated by using

$$\sigma_t = (MC)/I \tag{1}$$

where I is the moment of inertia, C is the distance from the neutral axis to the surface of the sample, and M is the applied four-point bending moment. Fracture strengths at the fracture origins (σ_f) were computed by using equation (1) with C as the distance from the neutral axis to the center of the fracture origin. Fracture toughness (K_{IC}) values were obtained from the relationship between fracture strength and flaw shape, size, and location (refs. 19 to 23). From reference 21, K_{IC} values were calculated by using the following relation

$$\sigma_f = \frac{Z}{Y} \frac{K_{IC}}{\sqrt{a}} \tag{2}$$

where σ_f is the fracture stress at the origin, a is the flaw depth for a surface flaw and half the diameter for a spherical subsurface flaw (equal to the minor axis for an ellipsoid), Z is the flaw shape parameter, and Y is a geometrical parameter equal to 2.0 and 1.77 (ref. 19) for surface and subsurface fracture origins, respectively, which are much smaller than the specimen dimension. The flaw shape parameter Z is the product of two independent, dimensionless parameters, Z_e and Z_d (refs. 20 and 21). The parameter Z_e varies with the flaw shape in the fracture plane and can be obtained from figure 2 in reference 20. The parameter Z_d varies with the ratio of the length of the radial crack extending from the flaw periphery in the fracture plane to the diameter of the pore or inclusion (ref. 21).

RESULTS

Fractography

Out of 25 specimens tested, 17 fracture origins were identifiable. The type, shape, size, and location of fracture origins are tabulated in table III. The 17 fracture origins identified were 5 bulk voids, 2 surface voids, 1 iron-rich inclusion, 1 large grain, 3 bulk agglomerates, and 5 surface agglomerates. SEM micrographs of typical fracture origins are presented in figure 3.

TABLE III. - ASSESSMENT OF FRACTURE ORIGINS

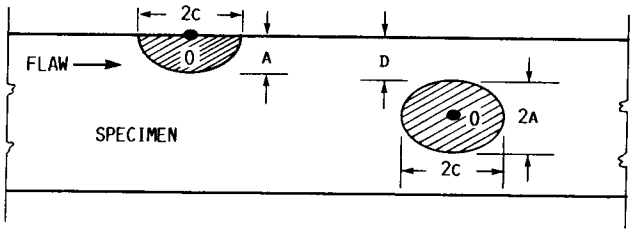

Batch number	Specimen number	Type	Shape	D,[a] μm	A[a] or 2A, μm	2C,[a] μm
1	3	Unidentified	----------	---	---	---
	5	Agglomerate	Circular	6	45	45
	8	Void	Irregular	14	69	69
	12	Agglomerate	Elliptical	60	40	70
	13	Void	Elliptical	40	80	104
2HP	2	Void	Semi-elliptical	0	19	67
	5	Agglomerate	Elliptical	12	65	127
	8	Void	Elliptical	120	58	92
	11	Unidentified	----------	---	---	---
	23	Agglomerate	Semi-elliptical	0	46	92
4	4	Void	Elliptical	50	69	127
	14	Void	Semi-elliptical	0	58	117
	15	Unidentified	----------	---	---	---
	16	Unidentified	----------	---	---	---
	18	Large Grain	Trapezoidal	7	34	58
4HP	1	Unidentified	----------	---	---	---
	5	Unidentified	----------	---	---	---
	8	Fe inclusion	Irregular	50	140	140
	9	Unidentified	----------	---	---	---
	24	Unidentified	----------	---	---	---
5HP	35	Agglomerate	Semi-elliptical	0	50	150
	36	Agglomerate	Irregular	0	35	55
	37	Agglomerate	Semicircular	0	30	200
	46	Void	Elliptical	120	100	120
	59	Agglomerate	Circular	0	60	60

[a]See sketch.

Detection of Fracture Origins

Acoustic microscopy. - The reduced-aperture focusing lens gave a maximum point-to-point resolution at the sample surface on the order of 100 μm. Large surface-breaking voids just below the lens resolution could be detected, though not acoustically resolved.

In the sample volume of interest, within a few hundred micrometers of the sample tensile surface, a strong surface reflection masked any subsurface defect signal present. The tail of the surface reflection signal interfered up to approximately 90 ns after the start of the input pulse. On the basis of the sound velocity in these bars, defects within about 500 μm from the scanned (tensile) surface were masked.

Scanning from the compression side, with the bulk sample volume of interest between the acoustic pulse source and the sample tensile surface, eliminates the surface masking and places the volume under evaluation away from the scanned surface. Additional material may be introduced between the acoustic lens and the sample volume of interest, however, depending upon the sample thickness. Inhomogeneities in the sample interior can mask features or complicate the interpretation of images from deep within the specimen. Figure 4 shows acoustic micrographs of SiC specimens where surface and subsurface flaws are imaged. Subsurface flaws as deep as 2 mm into the specimen were detected. For depths greater than 2 mm, side wall interference and material variations became more pronounced (fig. 4(d)). The SiC bars used in this study had an average thickness of 2.72 mm. Hence, these bars proved too thick for reliable critical defect detection in the immediate proximity of the surfaces.

Microfocus radiography. - Radiographic detectability results of fracture origins are tabulated in table IV. Dimensions of the fracture-causing flaws, as well as what they represent in terms of dimensional sensitivity in the width and the thickness directions, are also tabulated. Seven out of seventeen identified fracture origins were radiographically detected. All five bulk voids, one out of two surface voids, and the iron-rich inclusion were detected. All surface and subsurface agglomerates, and the large grain were missed. Figure 5 shows a black and white print of the radiographic film imaging the fracture origin (bulk void) in one of the sintered bars. In general the flaw size as it appeared on the radiograph was less than or equal to its real size as determined optically (table IV).

Flexural Strength and Fracture Toughness

Flexural test results (σ_t) are tabulated in table V. Because fracture origins can generally be determined 60 percent of the time (ref. 4), σ_t is used instead of σ_f in the analysis of ceramic strength. There is no reason to believe, on the basis of an f-test at the 95-percent confidence level (ref. 24), that the five batches differ in strength variability. Further, there is only reason to believe that the mean strength for batch 1 exceeds that of batch 4HP; otherwise no differences in mean strengths of all other batches are noted. This is substantiated by a t-test at the 95-percent confidence level (ref. 24).

Fracture toughness results are tabulated in table V. In this paper radial cracks were comparable to pore/agglomerate diameter, hence Z_d was taken to be equal to 1.0. Further, no ligament failure was noted to occur prior to catastrophic failure caused by a pore/agglomerate located beneath the surface. Where fracture origins were located up to 15 μm below the surface, these origins were treated as surface flaws, because the minimum surface flaw size needed for ligament failure to occur (ref. 20) was approaching

TABLE IV. - RADIOGRAPHIC DETECTION OF FRACTURE ORIGINS

[Specimen dimensions measured along thickness, T, width, W, and length, L. Flaw dimensions XT, XW, and XL measured along T, W, and L, respectively.]

Batch number	Specimen number	Type[a]	Optical flaw dimensions, μm		Sensitivity,[b] percent		Flaw detected		Radiographic flaw dimensions, μm	
			XT	XW	T	W	T	W	XW, XL	XT, XL
1	3	U	---	---	---	---	---	---	--------	--------
	5	BA	45	45	1.6	0.8	No	No	--------	--------
	8	BV	69	69	2.5	1.2	Yes	Yes	43, 85	43, 85
	12	BA	40	70	1.4	1.3	No	No	--------	--------
	13	BV	80	104	2.9	1.9	Yes	No	43, 43	--------
2HP	2	SV	19	67	0.7	1.2	No	No	--------	--------
	5	BA	65	127	2.4	2.3	No	No	--------	--------
	8	BV	58	92	2.1	1.7	Yes	No	63, 43	--------
	11	U	---	---	---	---	---	---	--------	--------
	23	SA	46	92	1.7	1.6	No	No	--------	--------
4	4	BV	69	127	2.5	2.3	Yes	No	105, 105	--------
	14	SV	58	115	2.1	1.6	Yes	Yes	105, 42	42, 105
	15	U	---	---	---	---	---	---	--------	--------
	16	U	---	---	---	---	---	---	--------	--------
	18	LG	34	58	1.2	1.0	No	No	--------	--------
4HP	1	U	---	---	---	---	---	---	--------	--------
	5	U	---	---	---	---	---	---	--------	--------
	8	FeI	140	140	5.3	2.5	Yes	Yes	62, 62	62, 62
	9	U	---	140	---	---	---	---	--------	--------
	24	U	---	140	---	---	---	---	--------	--------
5HP	35	SA	50	150	1.8	2.7	No	No	--------	--------
	36	SA	35	55	1.3	1.0	No	No	--------	--------
	37	SA	130	200	4.8	3.6	No	No	--------	--------
	46	BV	100	120	3.8	2.2	Yes	Yes	106, 64	106, 64
	59	SA	60	60	2.2	1.1	No	No	--------	--------

[a]U, unidentified; BA, bulk agglomerate; BV, bulk void; SA, surface agglomerate; SV, surface void; LG, large grain; FeI, iron inclusion.
[b]Sensitivity, 100(XT/T) or 100(XW/W).

TABLE V. - FLEXURAL STRENGTH AND FRACTURE TOUGHNESS RESULTS

Batch number	Specimen number	Fracture strength of tensile surface, σ_t, MPa	Fracture strength at origin, σ_f, MPa	$(\sigma_t)_{avg}$, standard deviation, MPa	Y/Z	Fracture toughness, K_{IC}, $MN \cdot m^{-3/2}$	$(K_{IC})_{avg}$, standard deviation, $MN \cdot m^{-3/2}$
1	3	356	---	338±48	---	---	3.26±0.26
	5	389	385		1.27	3.23	
	8	269	265		1.27	2.80	
	12	382	369		1.42	3.31	
	13	326	317		1.31	3.71	
2HP	2	319	319	319±52	1.60	2.23	2.88±0.65
	5	211	267		1.67	3.59	
	8	322	305		1.40	3.25	
	11	402	---		----	----	
	23	281	281		1.27	2.42	
4	4	265	256	315±40	1.44	3.06	3.22±0.39
	14	304	304		1.27	2.94	
	15	342	---		----	----	
	16	366	---		----	----	
	18	296	281		1.60	3.67	
4HP	1	251	---	273±51	----	----	---------
	5	334	---		----	----	
	8	209	201		----	----	
	9	306	---		----	----	
	24	271	---		----	----	
5HP	35	289	289	297±25	1.56	3.19	3.20+0.73
	36	324	324		1.25	2.40	
	37	288	288		1.25	4.10	
	46	319	298		1.26	3.75	
	59	264	264		1.26	2.57	

the average porosity value for the specific batch. On the basis of an f- and t-test at the 95-percent confidence level, all four batches did not differ in toughness variability or in mean toughness.

Ultrasonic Velocity and Attenuation

Average velocity based on three measurements at different locations in the MOR bar (fig. 2) was plotted as a function of bulk density for all 25 bars in figure 6. The data show that velocity is an increasing function of density. The average velocities are 1.184, 1.188, 1.169, 1.189, and 1.099 cm/μs for batches 1, 2HP, 4, 4HP, and 5HP, respectively. By comparing these results to corresponding average bulk densities, for a 1-percent change in density there is approximately a 1-percent change in velocity.

Attenuation coefficient results are plotted as a function of frequency for all five batches in figure 7. Plotted data are the measured attenuation at or very near the location where fracture took place. Dashed lines represent the boundary of the scatter in the frequency regime shown. They also represent the exact data for two out of the five specimens which comprised each batch. Attenuation coefficient in the frequency regime shown does differentiate substantially between batches, on the basis of their density and microstructural characteristics, as was demonstrated in previous work

(refs. 12 to 14). Further, figure 7 shows for every batch the average flexural strength and the average fracture toughness for the purpose of comparison with corresponding attenuation measurements.

DISCUSSION

Radiography and Acoustic Microscopy

The radiographic sensitivity to the voids detected ranged from 1.2 to 5.3 percent. But three of these voids were not detected through width with sensitivities of 1.7, 1.9, and 2.3 percent. In the case of the 2.3 percent sensitivity, film developing was the reason. In the other two cases, it is believed that missing these voids was due to material variations in the x-ray path and to the void morphology itself, where a void appears like an agglomerate, as shown in figure 3(c) for the 1.9 percent case. These results agree with previous work, where the sensitivity of the microfocus x-ray system was established by using seeded surfaces and internal voids (ref. 3). The surface void missed by x-rays represented a 0.7- and a 1.2-percent sensitivity in the thickness and width directions, respectively. These radiographic sensitivities are beyond the reliable detectability of the x-ray system (ref. 3).

On the basis of the results herein, we believe that in order to image fracture-causing flaws at or near the surface of MOR ceramic bars, a full-aperture lens and higher frequencies are needed. With a wide-aperture lens, the rays incident on the tensile surface at the Rayleigh angle should produce surface acoustic waves traveling on the surface of the specimen, leaking back into the water, and being collected by the lens (ref. 25). Voids and cracks normal to the specimen surface located within one Rayleigh wavelength of the surface will scatter these Rayleigh waves and affect the microscope signal (refs. 25 and 26). Operation at higher frequencies (100 to 200 MHz) would improve the resolution. In the case of subsurface flaws located away from the Rayleigh wave path, a shorter input pulse is needed to reduce the interference between the image pulse and the surface pulse.

Radiography proved useful in detecting high-density inclusions and isolated voids as fracture origins in SiC MOR bars, but failed to detect surface and subsurface low-density agglomerates and large grains as fracture-causing defects. This was expected, because low-density agglomerates are voidlike regions filled with material which reduces drastically the differential in x-ray absorption between the agglomerate and the matrix. Large grains do not present enough difference in density from the matrix in order to be detected. Acoustic microscopy, using a wide-angle acoustic lens, has potential for detecting large grains and low-density agglomerates located at or near the surface (ref. 25). This definitely merits further investigation.

The Role of Ultrasonic Velocity and Attenuation

For the carbide system investigated herein, a more direct correlation was found between velocity and density (fig. 6) than between flexural strength/fracture toughness and density (tables I and V). For example, comparing batch 1 (3.12 g/cm^3) to batch 5HP (2.92 g/cm^3), where average fracture

stress and fracture toughness are statistically the same for both, velocities were different (1.184 and 1.099 cm/μs, respectively). Velocity was not sensitive to changes in mean grain and pore size; that is, no substantial difference in velocity was detected between batch 4HP (1.189 cm/μs) and batch 1 (1.184 cm/μs), although batch 4HP had over twice the mean grain and pore size of batch 1.

Attenuation at or near the location where the fracture occurred agreed well with previous attenuation measurements from previous work (ref. 13). Further, attenuation dependency on net average porosity can be seen by comparing batch 4 and batch 4HP attenuation data, where a 1.6-percent difference in density (also a 1-percent difference in velocity) reflects a 56-percent difference in attenuation at a frequency of 100 MHz. The attenuation data for batches 5HP, 4, and 1 demonstrate that the dominant attenuation mechanisms are average pore size and net average porosity. There is no clear evidence of a grain boundary scattering mechanism in any of the five batches.

For batches 1 and 4HP, velocities and attenuation coefficients did not differ greatly, whereas the average strength for batch 1 exceeded that of batch 4HP, on the basis of t-test data at the 95-percent confidence level. This difference is probably due to different flaw populations that existed in these two batches. From radiography, 4HP had many high-density inclusions, while batch 1 had mainly void and agglomerate types of flaws.

Flexural stress and fracture toughness data demonstrated great scatter within batches, which made it difficult to discern common microstructural factors that affected both attenuation and fracture mechanics parameters. Although porosity and grain size dependence of strength and toughness are expected, the problem still remains that one dominant flaw can mask the effect of bulk porosity and microstructure on strength and toughness. Further, uncertainties associated with the shape and geometric factors (ref. 1) used in the toughness calculations might have masked the presence of this dependency. Herein, attenuation-toughness behavior is limited by shortcomings in K_{IC} determination, and a definitive statement cannot yet be made. Additional research is merited for full appreciation of the attenuation measurements in different frequency regimes, where different scatterers may be the common dominant attenuation and fracture mechanisms.

CONCLUSIONS

Projection microfocus x-radiography, ultrasonic velocity and attenuation, and reflection scanning acoustic microscopy were assessed for characterizing silicon carbide specimens. Radiography proved useful in detecting high-density inclusions and isolated voids, but failed in detecting surface and subsurface agglomerates and large grains as fracture origins. Ultrasonic velocity dependency on density was evident. Attenuation dependency on density and mean pore size was clearly demonstrated. Understanding attenuation as a function of toughness was limited by shortcomings in K_{IC} determination. The applicability of acoustic microscopy using a reduced-aperture focusing lens to detect near-surface flaws was limited, indicating the need for a full-aperture lens for near-surface failure-causing flaws.

REFERENCES

1. A.G. Evans, "Fracture Mechanics Determinations," pp. 17-48 in Fracture Mechanics of Ceramics, Vol. 1, Edited by R.C. Bradt, D.P.H. Hasselman, and F.F. Lange, Plenum Press, New York, 1974.

2. W.A. Ellingson, et al, "Characterization of Porosity in Green-State and Partially Densified Al_2O_3 by Nuclear Magnetic Resonance Imaging," To be published in Ceram. Eng. Sci. Proc., **8** [7-8] (1987).

3. G.Y.Baaklini, and D.J. Roth, "Probability of Detection of Internal Voids in Structural Ceramics Using Microfocus Radiography," J. Mater. Res., **1** [3] 457-467 (1986).

4. W.A. Sanders, and G.Y. Baaklini, "Correlation of Processing and Sintering Variables with the Strength and Radiography of Silicon Nitride," Ceram. Eng. Sci. Proc., **7** [7-8] 839-859 (1986).

5. D.J. Roth, and G.Y. Baaklini, "Reliability of Scanning Laser Acoustic Microscropy for Detecting Internal Voids in Structural Ceramics," Adv. Ceram. Mater., **1** [3] 252-258 (1986).

6. S.J. Klima, P.B. Abel, and G.Y. Baaklini, "Nondestructive Evaluation of Structural Ceramics," pp. 359-367 in Proceedings of the Twenty-Fourth Automotive Technology Development Contractors' Coordination Meeting, SAE, Warrendale, PA, 1986.

7. P.K. Khandelwal, and P.W. Heitman, "Photoacoustic Microscopy of Ceramic Materials for Heat Engines," pp. 901-907 in Ceramic Materials and Components for Engines, Edited by W. Bunk and H. Hausner, Verlag Deutsche Keramische Gesellschaft, Bad Honnef, 1986.

8. R.L. Thomas, L.D. Favro, P.K. Kuo, D.N. Rose, and D.C. Bryk, "Scanning Photoacoustic Microscopy of Aluminum with Aluminum Oxide, Roughness Standards, and Rubber," TACOM-TR-13077, July 1985. (Avail. NTIS, AD-A169160).

9. R.W. Rice, S.W. Freiman, R.C. Pohanka, J.J. Mecholsky Jr., and C.C. Wu, "Microstructural Dependence of Fracture Mechanics Parameters in Ceramics," pp. 849-876 in Fracture Mechanics of Ceramics, Vol. 4, Edited by R.C. Bradt, D.P.H. Hasselman, and F.F. Lange, Plenum Press, New York, 1978.

10. D.R. Biswas, and R. M. Fulrath, "Mechanical Properties of Porous PNZT Polycrystalline Ceramics," pp. 933-943 in Fracture Mechanics of Ceramics, Vol. 4, Edited by R.C. Bradt, D.P.H. Hasselman, and F.F. Lange, Plenum Press, New York, 1978.

11. R.W. Rice, "Fractographic Identification of Strength-Controlling Flaws and Microstructure," pp. 323-345 in Fracture Mechanics of Ceramics, Vol. 1, Edited by R.C. Bradt, D.P.H. Hasselman, and F.F. Lange, Plenum Press, New York, 1974.

12. S.J. Klima, and G.Y. Baaklini, "Nondestructive Characterization of Structural Ceramics," SAMPE Q., **17** [3] 13-19 (1986).

13. G.Y. Baaklini, E.R. Generazio, and J.D. Kiser, "High Frequency Ultrasonic Characterization of Sintered SiC," To be published in Ceram. Eng. Sci. Proc., **8** [7-8] (1987).

14. E.R. Generazio, D.J. Roth, and G.Y. Baaklini, "Imaging Subtle Microstructural Variations in Ceramics With Precision Ultrasonic Velocity and Attenuation Measurements," NASA TM-100129 (1987).

15. A. Vary, "Correlations Among Ultrasonic Propagation Factors and Fracture Toughness Properties of Metallic Materials," Mater. Eval., **36** [7] 55-64 (1978).

16. E.R. Generazio, "Determination of Grain Size Distribution Function Using Two-Dimensional Fourier Transforms of Tone Pulse Encoded Images," NASA TM-88790 (1986).

17. D.R. Hull, H.E. Kautz, and A. Vary, "Measurement of Ultrasonic Velocity Using Phase-Slope and Cross-Correlation Methods," Mater. Eval., **43** [11] 1455-1460 (1985).

18. E.R. Generazaio, "The Role of the Reflection Coefficient in Precision Measurement of Ultrasonic Attenuation," Mater. Eval., **43** [8] 995-1004 (1985).

19. W.F. Brown, Jr., and J.E. Srawley, Plane Strain Crack Toughness Testing of High Strength Metallic Materials. ASTM-STP-410, ASTM, Philadelphia, PA, 1967, pp. 1-15.

20. A.G. Evans, and G. Tapin, "Effects of Microstructure on the Stress to Propagate Inherent Flaws," Proc. Br. Ceram. Soc., No. 20, 275-297 (1972).

21. G.K. Bansal, and W.H. Duckworth, "Fracture Stress as Related to Flaw and Fracture Mirror Sizes," J. Am. Ceram. Soc., **60** [7-8] 304-310 (1977).

22. G.K. Bansal, "Effect of Flaw Shape on Strength of Ceramics," J. Am. Ceram. Soc., **59** [1-2] 87-88 (1976).

23. S.C. Danforth, and M.H. Richman, "Strength and Fracture Toughness of Reaction-Bonded Si_3N_4," Am. Ceram. Soc. Bull., **62** [4] 501-505 (1983).

24. M.G. Natrella, Experimental Statistics. NBS Handbook No. 91, National Bureau of Standards, Washington, D.C., 1963.

25. M. Nikoonahad, "Reflection Acoustic Microscopy for Industrial NDE," Chapter 7 in Nondestructive Testing, Vol. 7, Edited by R.S. Sharpe, Academic Press, New York, 1984.

26. I.R. Smith, R.A. Harvey, and D.J. Fathers, "An Acoustic Microscope for Industrial Applications," IEEE Trans. Sonics Ultrasonics, **32** [2] 274-288 (1985).

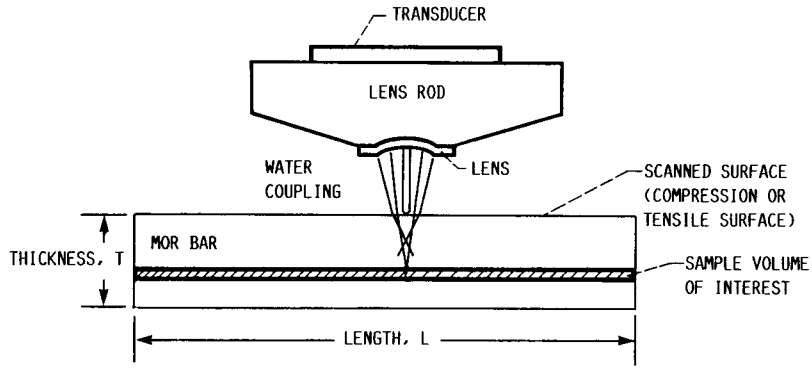

FIGURE 1. - SCHEMATIC DIAGRAM OF LENS-SPECIMEN CONFIGURATION FOR SCANNING ACOUSTIC MICROSCOPY. RAY PATHS FOR SURFACE REFLECTION AND ABERRATION SHOWN IN ADDITION TO FOCAL PLANE REFLECTION.

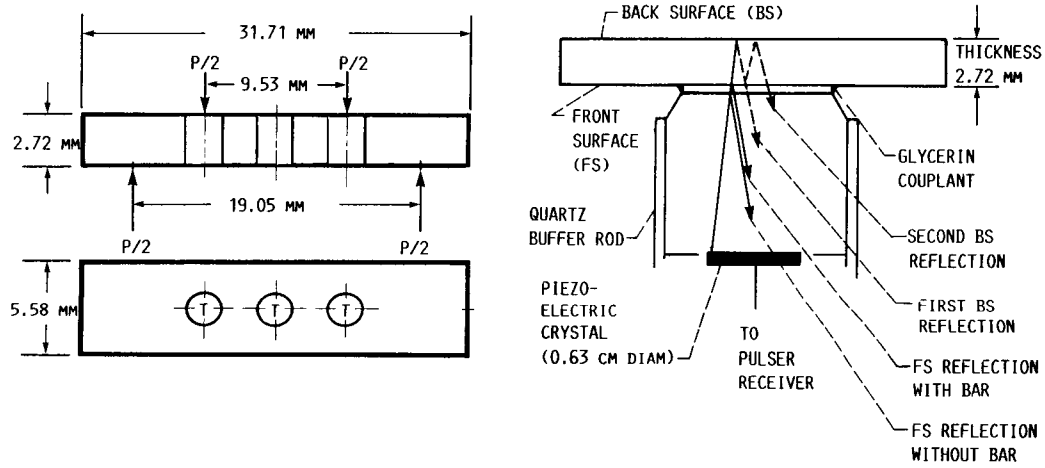

FIGURE 2. - PULSE-ECHO ULTRASONICS OF MOR BARS. LOCATION OF TRANSDUCER FOR ULTRASONIC MEASUREMENTS IS DENOTED BY T, AND P IS APPLIED LOAD.

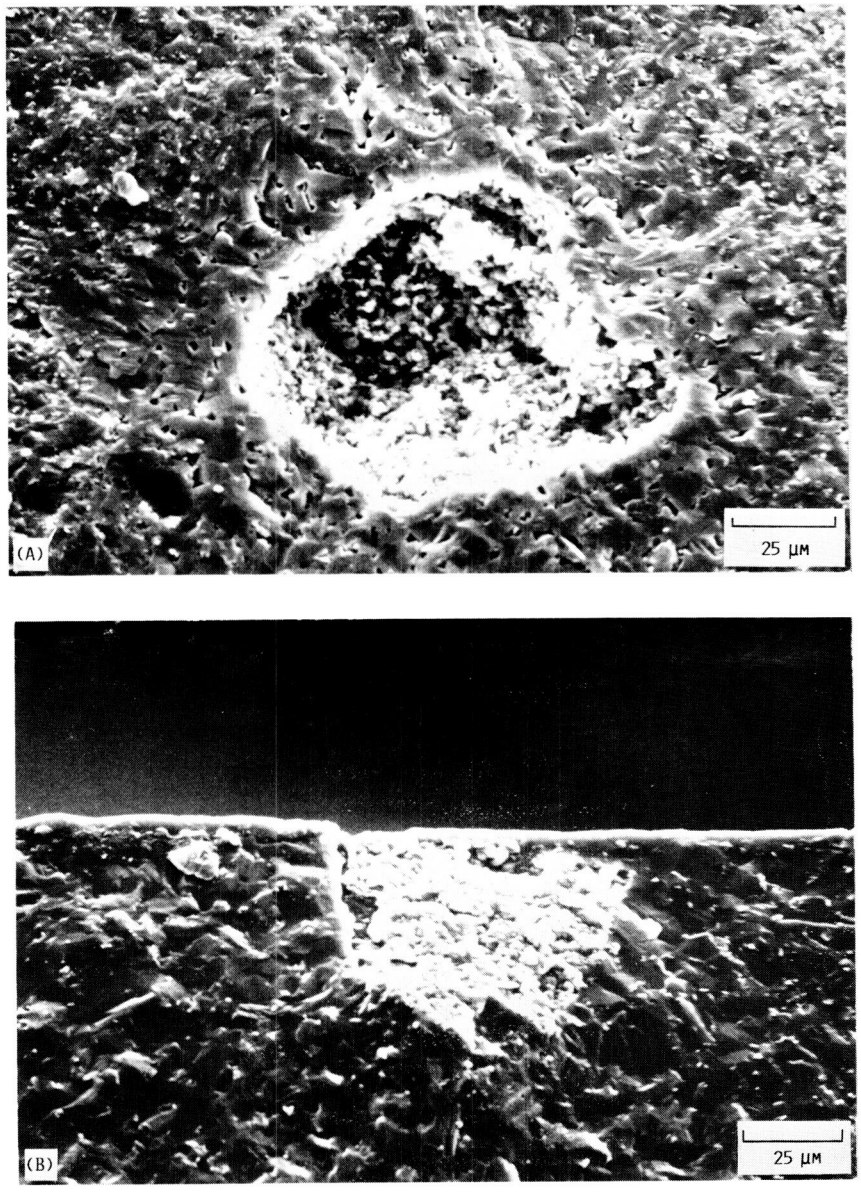

FIGURE 3. - SCANNING ELECTRON MICROGRAPHS OF FRACTURE ORIGINS IN SINTERED SiC MOR BARS. (A) BULK VOID, (B) SURFACE AGGLOMERATE, (C) BULK VOID (AGGLOMERATE-LIKE), AND (D) LARGE GRAIN.

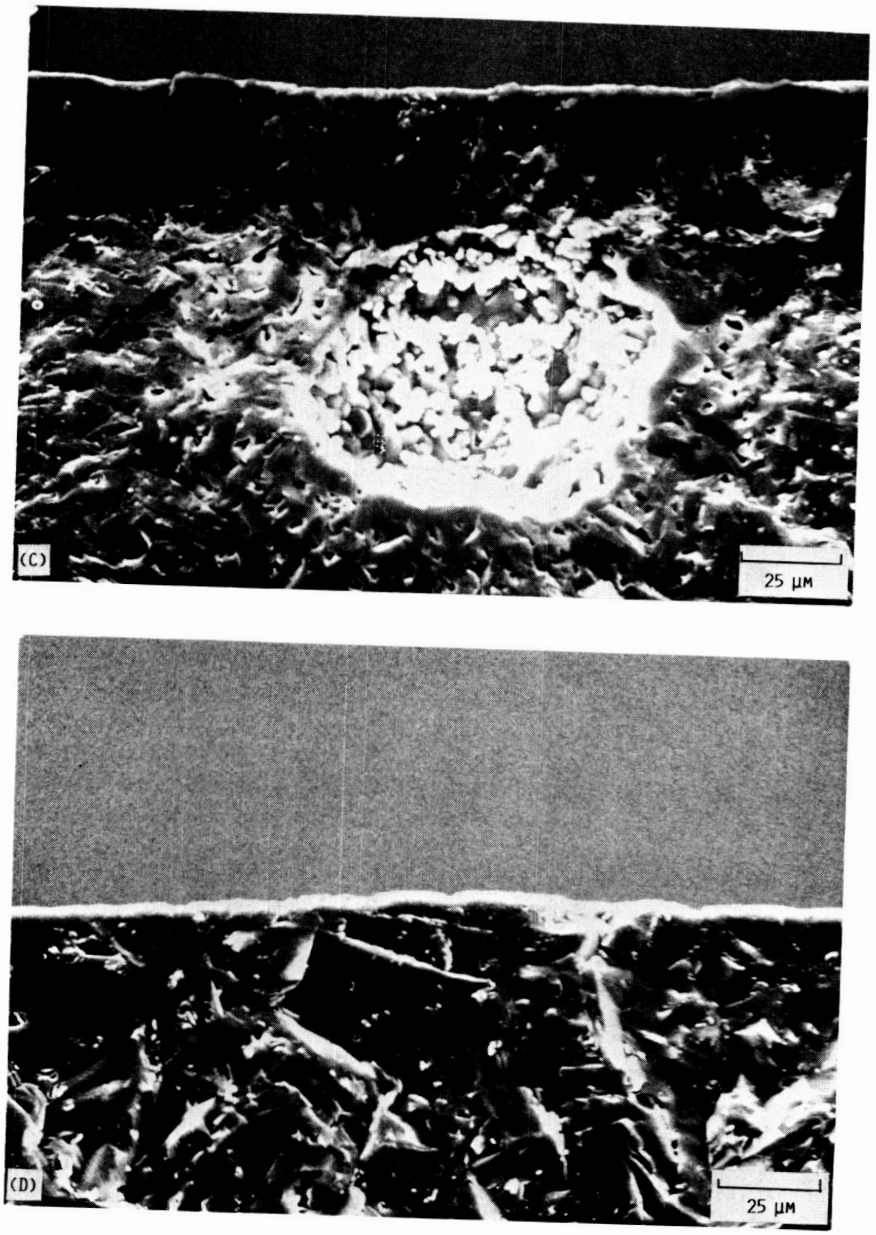

FIGURE 3. - CONCLUDED.

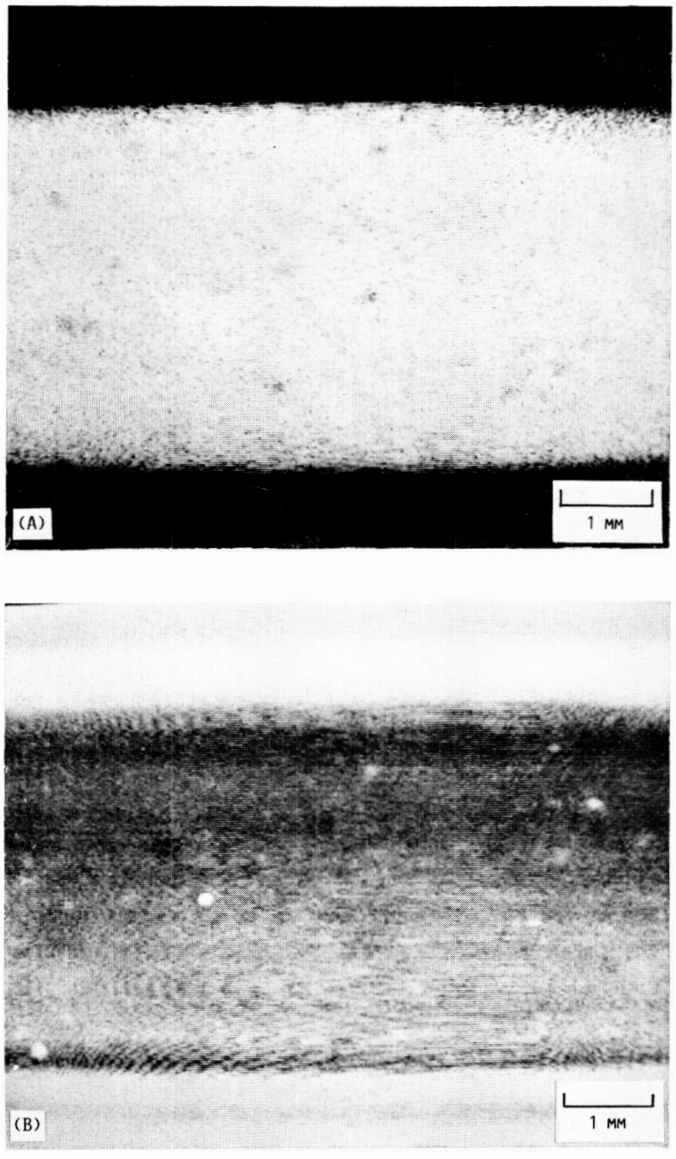

FIGURE 4. - ACOUSTIC MICROGRAPHS OF SiC SPECIMENS (NUMBERS 15 AND 4 OF BATCH 4) AT DIFFERENT FOCUS DEPTHS. (A) NUMBER 15, SURFACE; (B) NUMBER 15, 650 μm; (C) NUMBER 15, 1200 μm; AND (D) NUMBER 4, 2500 μm.

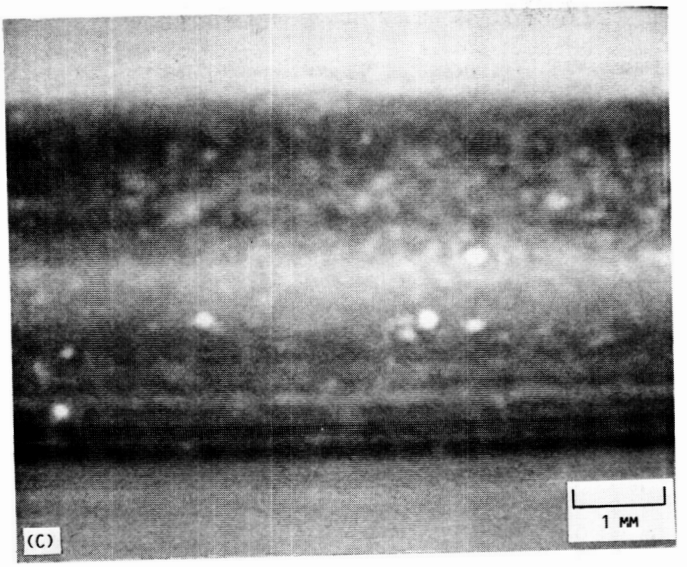

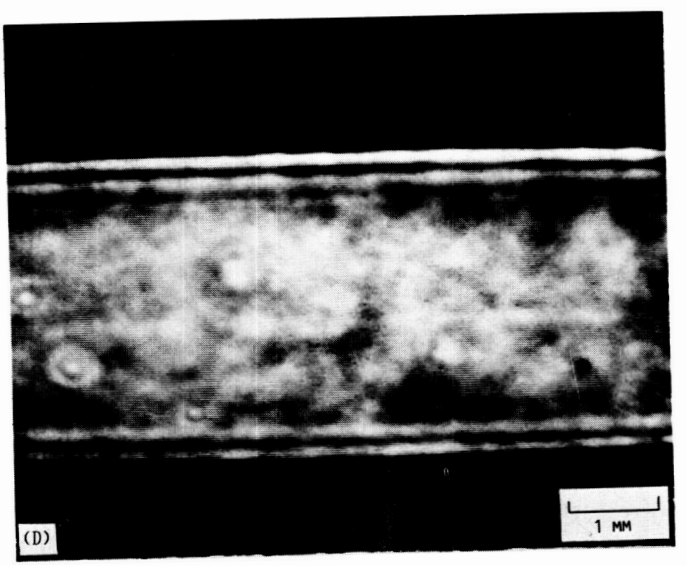

FIGURE 4. - CONCLUDED.

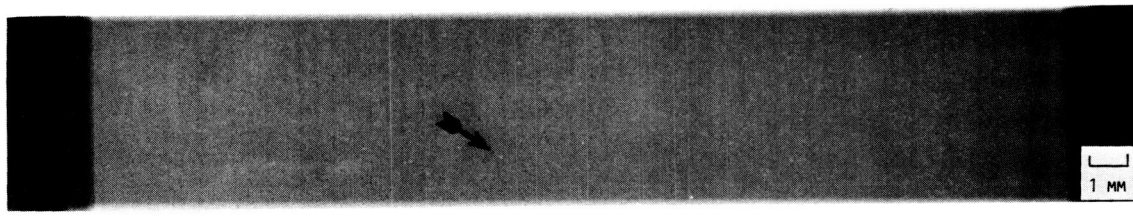

FIGURE 5. - MICROFOCUS RADIOGRAPH (W, L) OF SINTERED SiC BAR (NUMBER 4 OF BATCH 4). ARROW POINTS TO DETECTED FRACTURE ORIGIN (BULK VOID).

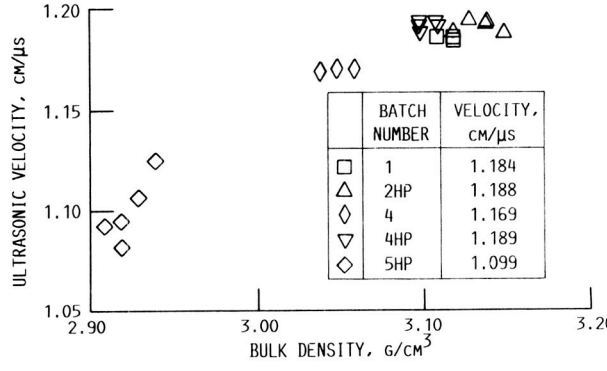

FIGURE 6. - ULTRASONIC VELOCITY AS FUNCTION OF BULK DENSITY FOR ALL FIVE BATCHES.

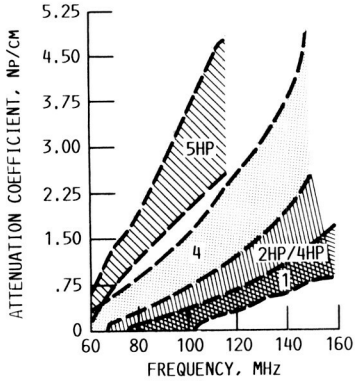

BATCH NUMBER	DENSITY, g/cm^3	MEAN PORE DIAMETER, μm	FLEXURAL STRENGTH, MPa	FRACTURE TOUGHNESS, MN · m$^{-3/2}$
1	3.12	1.60	338±48	3.26±0.37
2HP	3.14	1.63	319±52	2.88±0.65
4	3.05	3.82	315±40	3.22±0.39
4HP	3.10	3.44	273±51	---------
5HP	2.92	2.38	297±25	3.20±0.73

FIGURE 7. - COMPARISON OF ATTENUATION, FLEXURAL STRENGTH, AND FRACTURE TOUGHNESS.

NASA
National Aeronautics and Space Administration

Report Documentation Page

1. Report No.	2. Government Accession No.	3. Recipient's Catalog No.
NASA TM-100177		

4. Title and Subtitle
Flaw Imaging and Ultrasonic Techniques for Characterizing Sintered Silicon Carbide

5. Report Date

6. Performing Organization Code

7. Author(s)
George Y. Baaklini and Phillip B. Abel

8. Performing Organization Report No.
E-3753

10. Work Unit No.
533-05-11

9. Performing Organization Name and Address
National Aeronautics and Space Administration
Lewis Research Center
Cleveland, Ohio 44135-3191

11. Contract or Grant No.

13. Type of Report and Period Covered
Technical Memorandum

12. Sponsoring Agency Name and Address
National Aeronautics and Space Administration
Washington, D.C. 20546-0001

14. Sponsoring Agency Code

15. Supplementary Notes
Prepared for the Conference on Nondestructive Testing of High-Performance Ceramics, cosponsored by the American Ceramic Society and the American Society for Nondestructive Testing, Boston, Massachusetts, August 25-27, 1987. George Y. Baaklini, Cleveland State University, Cleveland, Ohio 44115; Phillip B. Abel, NASA Lewis Research Center.

16. Abstract
This investigation assessed the capabilities of projection microfocus x-radiography, ultrasonic velocity and attenuation, and reflection scanning acoustic microscopy for characterizing silicon carbide specimens. Silicon carbide batches covered a range of densities and different microstructural characteristics. Room-temperature, four-point flexural strength tests were conducted. Fractography was used to identify types, sizes, and locations of fracture origins. Fracture toughness values were calculated from fracture strength and flaw characterization data. Detection capabilities of radiography and acoustic microscopy for fracture-causing flaws were evaluated. Applicability of ultrasonics for verifying material strength and toughness was examined.

17. Key Words (Suggested by Author(s))	18. Distribution Statement
Nondestructive testing/evaluation; Ultrasonics; Radiography; Velocity; Attenuation; Ceramics; Fractography; Fracture toughness; Flexural strength; Acoustic microscopy	Unclassified - Unlimited Subject Category 38

19. Security Classif. (of this report)	20. Security Classif. (of this page)	21. No of pages	22. Price*
Unclassified	Unclassified	19	A02

*For sale by the National Technical Information Service, Springfield, Virginia 22161